nature communications

Article

https://doi.org/10.1038/s41467-024-53465-1

Carbon nanolayer-mounted single metal sites enable dipole polarization loss under electromagnetic field

Received: 24 April 2024

Accepted: 14 October 2024

Published online: 21 October 2024

Check for updates

Siyao Cheng[1,2,7], Daohu Sheng[3,7], Soumya Mukherjee[4], Wei Dong[3], Yuanbiao Huang[2], Rong Cao[2], Aming Xie[1] ✉, Roland A. Fischer[5] & Weijin Li[6] ✉

Surface modulation strategies have spurred great interest with regard to regulating the morphology, dispersion and flexible processability of materials. Unsurprisingly, customized modulation of surfaces is primed to offer a route to control their electronic functions. To regulate electromagnetic wave (EMW) absorption applications by surface engineering is an unmet challenge. Thanks to pyrolyzing surface-anchored metal-porphyrin, here we report on the surface modulation of four-nitrogen atoms-confined single metal site on a nitrogen-doped carbon layer (sM(N_4)@NC, M = Ni, Co, Cu, Ni/Cu) (sM=single metal; NC= nitrogen-doped carbon layer) that registers electromagnetic wave absorption. Surface-anchored metal-porphyrins are afforded by attaching them onto the polypyrrole surface via a prototypical click reaction. Further, sM(N_4)@NC is experimentally found to elicit an identical dipole polarization loss mechanism, overcoming the handicaps of conductivity loss, defects, and interfacial polarization loss among the current EMW absorber models. Importantly, sM(N_4)@NC is found to exhibit an effective absorption bandwidth of 6.44 and reflection loss of −51.7 dB, preceding state-of-the-art carbon-based EMW absorbers. This study introduces a surface modulation strategy to design EMW absorbers based on single metal sites that enable fine-tunable and controlled absorption mechanism with atomistic precision.

The advent of 5G era has ushered in high-frequency communication devices. This has massively spiked electromagnetic wave (EMW) surrounding mankind, resulting in high EMW pollution. This has identified to potentially cause a wide range of human health detriments, including reducing the quality of sleep, generating cumulative biological electromagnetic effects and leading to tissue damage[1–3]. Further, amplified EMW levels interfere with several high-precision instruments' functions. Developing EMW absorbers with high absorption performance offers a direct solution to these handicaps[4–6]. The EMW absorption performances are directly linked to their conductive, magnetic and dielectric properties since losses to the latter three are considered as the main EMW attenuation modes[7,8]. Among the several EMW attenuation modes, interfacial polarization, dipolar polarization, conduction loss, defect-induced polarization are all

[1]School of Safety Science and Engineering, Nanjing University of Science and Technology, Nanjing, PR China. [2]State Key Laboratory of Structural Chemistry Fujian Institute of Research on the Structure of Matter, Chinese Academy of Sciences, Fuzhou, PR China. [3]School of Chemistry and Chemical Engineering, Nanjing University of Science and Technology, Nanjing, PR China. [4]Bernal Institute, Department of Chemical Sciences, University of Limerick, Limerick V94 T9PX, Ireland. [5]Chair of Inorganic and Metal-Organic Chemistry, Department of Chemistry & School of Natural Sciences, Technical University of Munich, Lichtenbergstrasse 4, Garching, Germany. [6]School of Materials Science and Engineering, Nanjing University of Science and Technology, Nanjing, PR China. [7]These authors contributed equally: Siyao Cheng, Daohu Sheng. ✉e-mail: xieaming@njust.edu.cn; wjli@njust.edu.cn

categorized as dielectric loss modes[9–11]. Considering these EMW loss mechanisms, libraries of several EMW-absorbing materials have come to the fore lately, largely thanks to the various strategies to eliminate electromagnetic waves. For instance, a number of composites or hybrids have been developed to improve impedance matching and to address conductivity. Relying upon synergistic loss mechanisms, these hybrids could enhance the EMW absorption[12–14]. Following an alike synergy of mechanisms, interfacial strategies based on core-shell structures and heterostructures have also been proposed to deliver EMW absorbers with efficient EMW absorption capacity[15,16]. However, researchers often focus on material synthesis that tends to suffer from ambiguity in their underlying mechanisms. Conversely, introducing a model that critically interrogates in-depth mechanisms remains underreported in this area[17–20].

Thanks to the intrinsic dipole moments of molecules and/or atoms, clusters comprised of several atoms are generally considered as a model. Effected by a single variable principle of controlling dipole moments to tune the polarization, this approach reveals the polarization losses occurring from multiple loss mechanisms, in tandem[17–19]. For example, researchers have recently fabricated atomic-scale composites, e.g., Co single-atom sites, Co clusters and Co nanoparticles on nitrogen-doped graphene carbon, where regulating Co concentration and temperature enabled to control the dipole polarization loss and relaxation[20]. The relaxation model in Co clusters surrounded by single-atomic Co composites can be marked with negligible losses in conductivity and interfacial polarization. However, classification of dipole polarization/relaxation and EMW attenuation paths remain a matter of conjecture.

Theoretical and experimental data, in unison, suggest that EMW absorption often occurs either on the surface or on the micro/nanoscale interfaces of the absorbing materials[21,22]. However, the current models are handicapped with regard to experimentally clarifying the surface EMW attenuation paths or the micro/nano interface EMW attenuation paths. Integration of molecular crystals onto solid surfaces via surface modulation strategies (e.g., surface-mounted metal-organic frameworks, SURMOFs) have spurred great interest, thanks to their amenability to bottom-up control over the crystallites' morphological natures (such as size- and shape-regulation in crystals), dispersion, crystal facets and adaptable processability. The complexity of dynamism observed in most of these parameters underpins the high importance of the chemists' ability to regulate the electronic functions, bottom-up[23–25]. However, surface modulation engineering remains an uncharted territory as regards incubating a dipole polarization loss-driven mechanism in EMW absorption.

Benefiting from high surface free energy and approximately 100% atom utilization efficiency, surface-anchored single metal sites (sMs) have commanded substantial interest in the areas of electronics and electro-/photocatalysis[26–28]. However, single sMs are difficult to obtain via normal high-temperature synthesis because metal atoms tend to aggregate at high temperatures and form metal clusters/nanoparticles. Introducing constraints to single metal sites pre-dispersed with precursors is to prevent those single atoms/sites from aggregation[29,30]. The likely solution lies in choosing the right precursors with the right constraints pertaining to the single atoms (or single metal sites), in order to culminate in high EMW performances.

Harnessing the metal-nitrogen coordinated struts in metal-porphyrins, here we report on the surface modulation of N_4 on a nitrogen-doped carbon layer (sM(N_4)@NC, M = Ni, Cu, Co and Ni/Cu) to deliver EMW absorption. Pyrolysis of click reaction based surface anchoring of metal-porphyrins onto polypyrrole is the key step. The covalently bonded metal-porphyrins onto polypyrroles ensure monodispersity of the metal sites and prevents the sM(N_4) from agglomeration during subsequent high-temperature pyrolysis. This stems from the stronger nature of the covalent bonds. The sM(N_4) dipole in sM(N_4)@NC contributes the dominant loss mechanism with regard to its absorption performance. Based on the differences in electronegativity and intrinsic sM(N_4) dipole moments resulting in differential charges and varying polarizabilities, tweaking the metals allows us to fine-tune the EMW absorption abilities of sM(N_4)@NCs. More importantly, the obtained sM(N_4)@NC exhibits an effective absorption bandwidth and minimum reflection loss that is more than 1.5 times than that of state-of-the-art single atoms and carbon-based materials. In this study, we elegantly build a unique EMW dipole dominated loss model excluding other redundant EMW loss (e.g., conductivity, defects, and interfacial polarization loss) with promising EMW absorption properties, providing an approach for the design and in-depth loss study of EMW absorbers. Such approach focuses on the simply surface-mounted single atoms onto economic-budgeted and industrially practical carbon materials, opening an avenue for exploring future academic studied and industrial applicable EMW absorbing materials.

Results

Initially, a click-constrained strategy was used to conjugate the carboxyl-functionalized metal-ligand porphyrins (MPor, M = Ni, Cu, Co and Ni/Cu) to the secondary amine (-NH) on the surface of the $HMoO_3$ supported polypyrrole via a carbonyl to amide conversion reaction (Fig. 1a). The synthesis of $HMoO_3$-supported polypyrrole is described in the supporting information (Supplementary Fig. 1). $HMoO_3$, known as proton-hydrogenated MoO_3 (abbreviated as HMO), is taking the functions as a support in this system, providing a structured environment which could further mitigate the formation of amorphous regions of pyrrole during polymerization and enhance the consistency of the material properties. As shown in Fig. 1b, the presence of amide bonds is corroborated by Fourier-transform infrared spectroscopy (FTIR) data, wherein a peak at 1647 cm^{-1} (for sNi(N_4)@PPy) corresponds to the amide I band ($\nu_{C=O}$), suggesting the covalently bonded nature of polypyrrole surface to NiPor. This constrains the single metal sites (sM) to the material surfaces. Following the click reaction, the precursor was annealed at 700 °C to afford surface-modulated, 4-nitrogen surrounded single metal sites on a nitrogen-doped carbon layer, referred to as sM(N_4)@NC, M = Ni, Cu, Co and Ni/Cu. Powder X-ray diffraction (PXRD) patterns and Raman spectra of sM(N_4)@NC did not present characteristic peaks corresponding to metallic Ni or any other Ni compounds due to the low Ni contents not encountered traditionally (Supplementary Fig. 2). There are only two characteristic peaks observed in the Raman spectra. One is a D peak centered at 1340 cm^{-1} and a G peak centered at 1576 cm^{-1}, indicating graphitic structural defects and structures, respectively (Supplementary Fig. 3). Defect densities of all samples were expressed by I_D/I_G values. It can be observed that the I_D/I_G values are in the order of HMO@PPy (0.92) < HMO@NC (1.08) < sNi(N_4)@NC-1 (1.10), suggesting that introducing Ni atoms leads to alteration in charge distribution of the carbon layer, in effect, resulting in more defects[31,32].

Considering sNi(N_4)@NC-1 as a prototype, an in-depth study of its composition, morphology and structure was conducted. TEM images of sNi(N_4)@NC-1 exhibit a nanorod core-shell structure, similar to that of HMO@NC. Besides, atomic resolution high-angle annular dark-field scanning TEM (HAADF-STEM) images confirmed the absence of any agglomerated Ni component on the surface carbon layer (Supplementary Fig. 4). The corresponding energy dispersive spectroscopy-STEM (STEM-EDS) mapping demonstrates that C, N, and Ni elements of sNi(N_4)@NC-1 are uniformly dispersed across the HMO (Supplementary Fig. 4). Further, given that HMO materials dissolve in the solvent as molecular clusters under high-temperature conditions[33–35], we conducted the amide formation reaction at three different temperatures, *viz.*, 60 °C, 80 °C, and 100 °C. This led to morphological changes (to varying extents) in sNi(N_4)@NC-2, sNi(N_4)@NC and sNi(N_4)@NC-3 monitored through TEM and STEM-EDS studies (Supplementary Figs. 5–7). The rod-like morphology of sNi(N_4)@NC-2 gradually shrinks; sNi(N_4)@NC completely transitions to capsule shape with a

https://doi.org/10.1038/s41467-024-53465-1

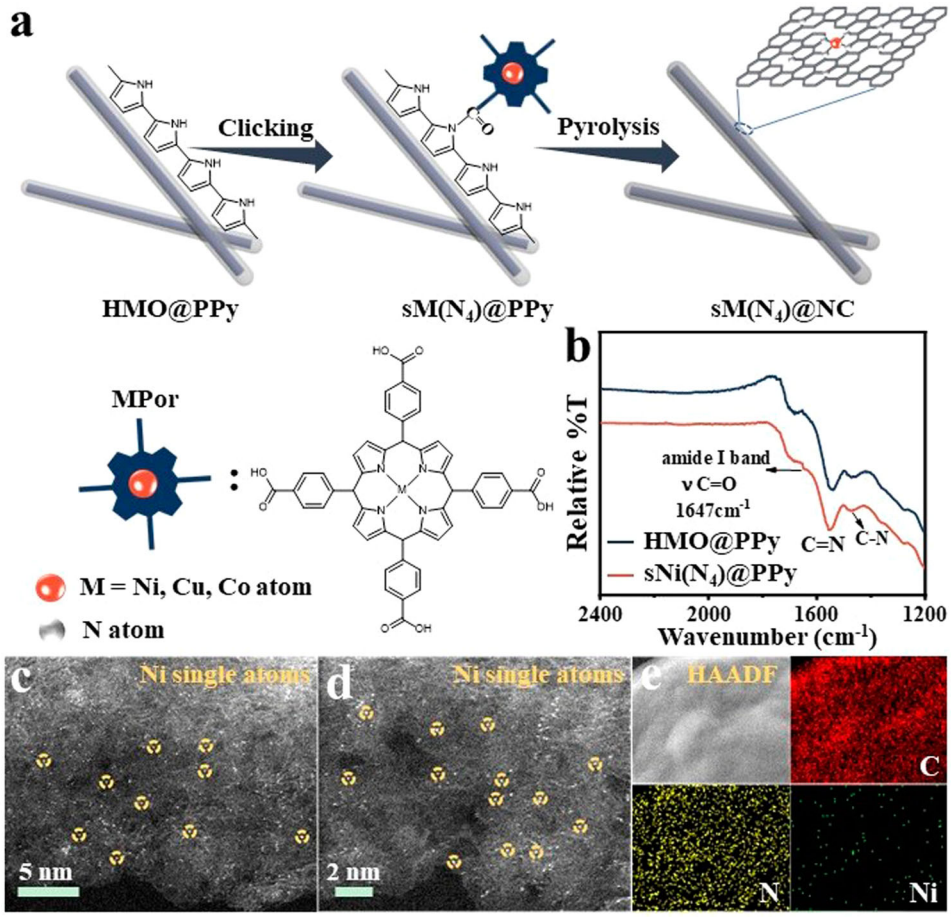

Fig. 1 | Synthesis and Characterization of sM(N_4)@NC. a Schematic illustrating the surface modulation of 4-nitrogen surrounded single metal sites on a nitrogen-doped carbon layer ((HMO represents hydrotreated MoO_3, MPor represents metal porphyrin, exemplified across the sM(N_4)@NC family, M = Ni, Cu, Co and Ni/Cu); (**b**) FTIR spectra of HMO@PPy and sNi(N_4)@PPy (T% represents a relative value); (**c**, **d**) Aberration-corrected high-angle annular dark-field scanning TEM images of sNi(N_4)@NC-3 and (**e**) corresponding EDX mapping of C, N, Ni.

significantly reduced HMO core; whereas, in sNi(N_4)@NC-3, the HMO is almost entirely dissolved, resulting in a hollow nanorod structure. From HAADF-STEM, it was observed that in sNi(N_4)@NC-2, sNi(N_4)@NC, and sNi(N_4)@NC-3, elemental Ni did not appear on the carbonaceous surface as clusters or nanoparticles due to the low Ni content (Supplementary Fig. 8). These results unequivocally indicate that the click-constraint strategy has uniformly anchored single metal atoms to the precursor at an atomic scale, and resolved the issue of metal atom aggregation during the pyrolysis process.

Additionally, the aberration-corrected high-angle annular dark-field scanning transmission electron microscopy (AC-HAADF-STEM) images exhibited uniform dispersion of bright dots over the prepared samples surface (Fig. 1c, d and Supplementary Fig. 9). Simply put, these dots correspond to the heavy Ni atoms and uniformly dispersed on the surface of carbon (Fig. 1e). Quantification of Ni was conducted by Inductively Coupled Plasma Optical Emission Spectrometer (ICP-OES) (Supplementary Fig. 10). Notably, the loading amount of Ni increases as the reaction temperature increases (Supplementary Table 1). Due to low metal loading, it is difficult to assign chemical state(s) to the carbon-supported Ni atoms using X-ray photoelectron spectroscopy (XPS) fitting spectra, where an ultralow signal-to-noise ratio renders the metal XPS profile meaningless (Supplementary Fig. 11). Ex-situ X-ray absorption fine structure (XAFS) spectrometry was performed to further reveal details of the Ni atomic structures in sNi(N_4)@NC-1 (see Supplementary Table 2 for the detailed coordination numbers, bond distances, Debye–Waller factors and inner potential correction). The K-edge absorption edge position of sNi(N_4)@NC-1 is located between Ni-foil and the pristine NiPc, but is closer to those of NiPc. This indicates the isolated Ni atoms to be carrying positive charge each, and the valence state of isolated Ni atoms to be close to +2 each (Fig. 2a)[36]. The Fourier transform of the k^3-weighted extended X-ray absorption fine structure (FT-EXAFS) spectra of sNi(N_4)@NC-1 displays one main peak at about 1. 48 Å, similar to the Ni-N peak in NiPc (Fig. 2b). sNi(N_4)@NC-1 does not exhibit characteristic peaks corresponding to Ni-O (2.54 Å) and Ni-Ni (2.17 Å), which further confirms that neither the Ni present in the pyrolyzed sNi(N_4)@NC-1 undergo oxidative aggregation nor did they form clusters, consistent with the HAADF-STEM results (Fig. 1c–e). The corresponding FT-EXAFS fitting results indicate that the Ni present in sNi(N_4)@NC-1 is coordinated to four nitrogen atoms (Fig. 2c, Supplementary Table 2). Moreover, the XAFS results show that the Ni atomic structure of sNi(N_4)@NC-2, sNi(N_4)@NC and sNi(N_4)@NC-3 is similar to sNi(N_4)@NC-1 (Supplementary Fig. 12). As shown in high-resolution N1s spectra, N in sNi(N_4)@PPy contains –N= (397.8 eV), –NH– (399.8 eV), and –NH^+– (400.9 eV), which are converted to pyridine N (398.8 eV), pyrrole N (400.7 eV), and graphite N (401.5 eV) after pyrolysis (Supplementary Fig. 13)[37]. Pyridine N to pyrrole N are found to be present in 1.36:1 proportion, according to their respective integral area ratios (Supplementary Table 3). Considering that the sNi(N_4)@NC-1 is mainly comprised of Ni–N_4, it is reasonable to deduce that the coordinated N atoms should stem from the pyrrole and pyridine functional groups. Moreover, Wavelet transform EXAFS (WT-EXAFS) functions as a good supplement for FT-EXAFS, owing to the former's powerful resolution in both k and R spaces. The wavelet transform (WT) plot of sNi(N_4)@NC-1 illustrates the WT maximum at 4.5 $Å^{-1}$,

https://doi.org/10.1038/s41467-024-53465-1

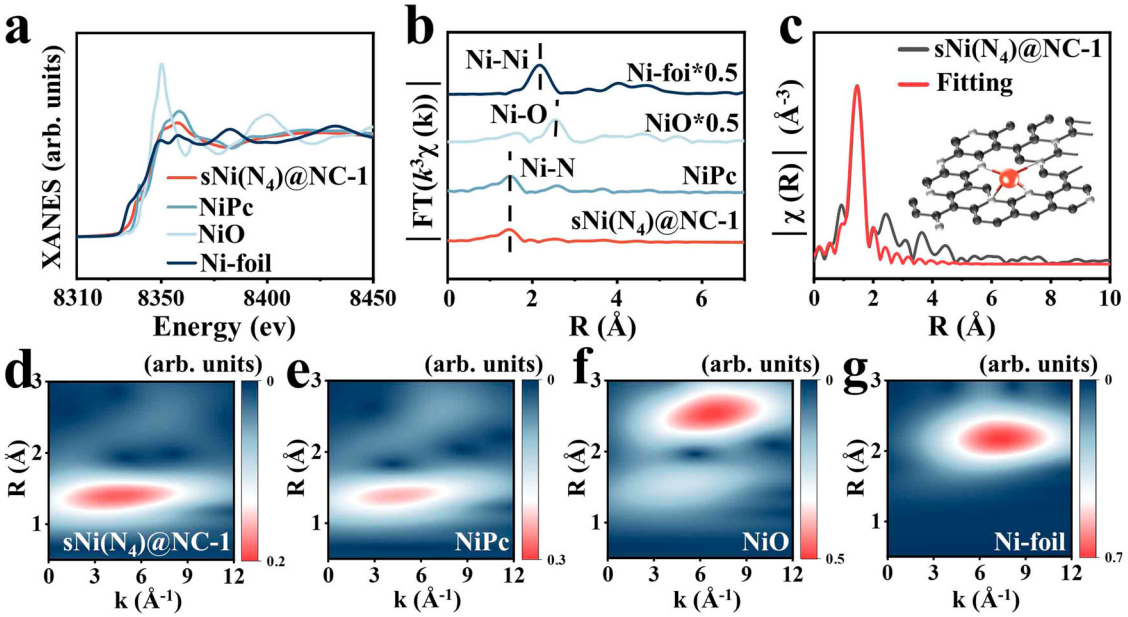

Fig. 2 | Synchrotron X-ray absorption spectrum characterization. a XANES spectrum at the Ni K-edge, (**b**) EXAFS spectra in reciprocal space, (**c**) EXAFS fitting results of sNi(N_4)@NC-1 (Inset: illustration of the sNi(N_4)). Wavelength transformations observed in (**d**) sNi(N_4)@NC-1, (**e**) NiPc, (**f**) NiO, and (**g**) Ni-foil.

corresponding to Ni−N bonding, upon comparing with Ni foil, NiO, and NiPc. No intensity maximum corresponding to Ni−Ni and Ni-O were observed (Fig. 2d–g), consistent with the EXAFS results. Additionally, the distribution of Ni(N_4) in sNi(N_4)@NC in reciprocal space (R space) is more dispersed compared to NiPC, indicating that the Ni(N_4) bonds in sNi(N_4)@NC have longer bond lengths, accompanied by an enhancement in electron delocalization[38,39], Electron paramagnetic resonance (EPR) could indicate the topological defects of the materials produced by the unpaired electrons, which are sensitive to external magnetic fields. sNi(N_4)@ NC-1 exhibits a stronger symmetry peak at about 350 mT (Supplementary Fig. 14a), indicating the existence of abundant unpaired electronic structures resonated under the action of external magnetic fields[39]. Besides, the Raman and XPS spectra of sNi(N_4)@NC-1 also show the presence of the defects (Supplementary Fig. 14b, c). These defects promote the electron density of the Ni(N_4) structure to be reindexed and lead to the central electron asymmetry of Ni(N_4), which enhance its polarizability under electromagnetic field[40].

The impact of introducing sNi(N_4) on the EMW absorption performance was evaluated through electromagnetic parameters, including the relative complex permittivity ($\varepsilon_r = \varepsilon' - j\varepsilon''$) and permeability ($\mu_r = \mu' - j\mu''$). Here, the real parts (ε' and μ') and the imaginary parts (ε'' and μ'') represent the ability to store and dissipate electromagnetic energy, respectively[41]. The filler ratio of all samples in the paraffin wax was controlled to be 40 wt%. The real (μ') and imaginary (μ'') values of sNi(N_4)@NC and sNi(N_4)@NC-X (X = 1, 2, 3) were found to be *ca.* 1 and 0, an artefact of the nonmagnetic nature of these samples (Supplementary Fig. 15)[42]. Therefore, for EMW absorption, the magnetic loss with Ni single atoms can be neglected. This conclusion can also be confirmed by its low magnetic loss angular tangent ($\tan\delta_\mu = \mu''/\mu'$) (Supplementary Fig. 16). As shown in Fig. 3a, d and Supplementary Fig. 17a, b, introducing single Ni sites leads to significant changes in the overall energy storage and consumption capacities, as well as brings about a noticeable increase in the dielectric loss of the HMO@NC material. According to the Debye theory, the semicircle observed in the Cole-Cole plot corresponds to the polarization relaxation process, while the straight tail represents the conduction loss. As shown in Supplementary Fig. 18, it is evident that the dielectric losses of HMO@NC, sNi(N_4)@NC-1, sNi(N_4)@NC-2, sNi(N_4)@NC and sNi(N_4)@NC-3 are attributed to the conduction loss and polarization relaxation process. When the Ni content increases, the samples exhibit higher slopes at the tail of the Cole-Cole curves as well as more semicircles, implying the existence of conduction loss and polarization loss. The more semicircles mean more polarization relaxation processes occur in the alternating electromagnetic field with favorable EMW absorption. To further investigate the underlying cause of increased dielectric loss in samples with sNi(N_4), the conduction loss ($\varepsilon_c'' = \sigma/\omega\varepsilon_0$, where σ, ω, and ε_0 are the electrical conductivity, the angular frequency, and the vacuum permittivity, respectively) was evaluated[43]. The intrinsic conductivity values of HMO@NC (0.165 S/m), sNi(N_4)@NC (0.234 S/m), sNi(N_4)@NC-60 (0.251 S/m), sNi(N_4)@NC-80 (0.274 S/m), and sNi(N_4)@NC-100 (0.328 S/m) are presented in Supplementary Fig. 19. The significant increase in conductivity for sNi(N_4)@NC-100 can be ascribed to the complete dissolution of the semiconductor HMO within it, resulting in faster electron transport. The ε_c'' values of sNi(N_4)@NC-1, sNi(N_4)@NC-2, and sNi(N_4)@NC are slightly higher than that of HMO@NC (Fig. 3c and Supplementary Fig. 17c). These results suggest that a slight increase in conduction loss when a small amount of Ni atoms is introduced. Based on the ε_c'' values, the polarization relaxation loss ($\varepsilon_p'' = \varepsilon'' - \varepsilon_c''$) of all the samples are determined[44]. As shown in Fig. 3d and Supplementary Fig. 17d, it can be seen that the ε_p'' values of sNi(N_4)@NC-1, sNi(N_4)@NC-2, sNi(N_4)@NC, and sNi(N_4)@NC-3 are significantly higher than that of HMO@NC, suggesting that introducing Ni single atoms increases the dipole polarization loss of the HMO@NC matrix material. Based on the above discussion, it can be concluded that the increase in polarization loss is the dominant reason for the increase in dielectric loss of sNi(N_4)@NC.

The controllable Ni atom concentration can result in tunable polarization behaviors, making the HMO@NC with Ni dipoles amenable to EMW absorption modulation. Upon increasing the concentration of single Ni sites, the prepared materials exhibit an increased minimum reflection loss (RL) values and maximum effective absorption bandwidth of −17.8 dB and 4.7 GHz (sNi(N_4)@NC-1), −36.3 dB and 5.6 GHz (sNi(N_4)@NC-2), −52.7 dB and 6.08 GHz (sNi(N_4)@NC), respectively (Fig. 3e, f; Supplementary Figs. 20–22, Supplementary Table 4). These results indicate that the modification of single Ni site on the surface could entirely alter the EMW absorption properties of

https://doi.org/10.1038/s41467-024-53465-1

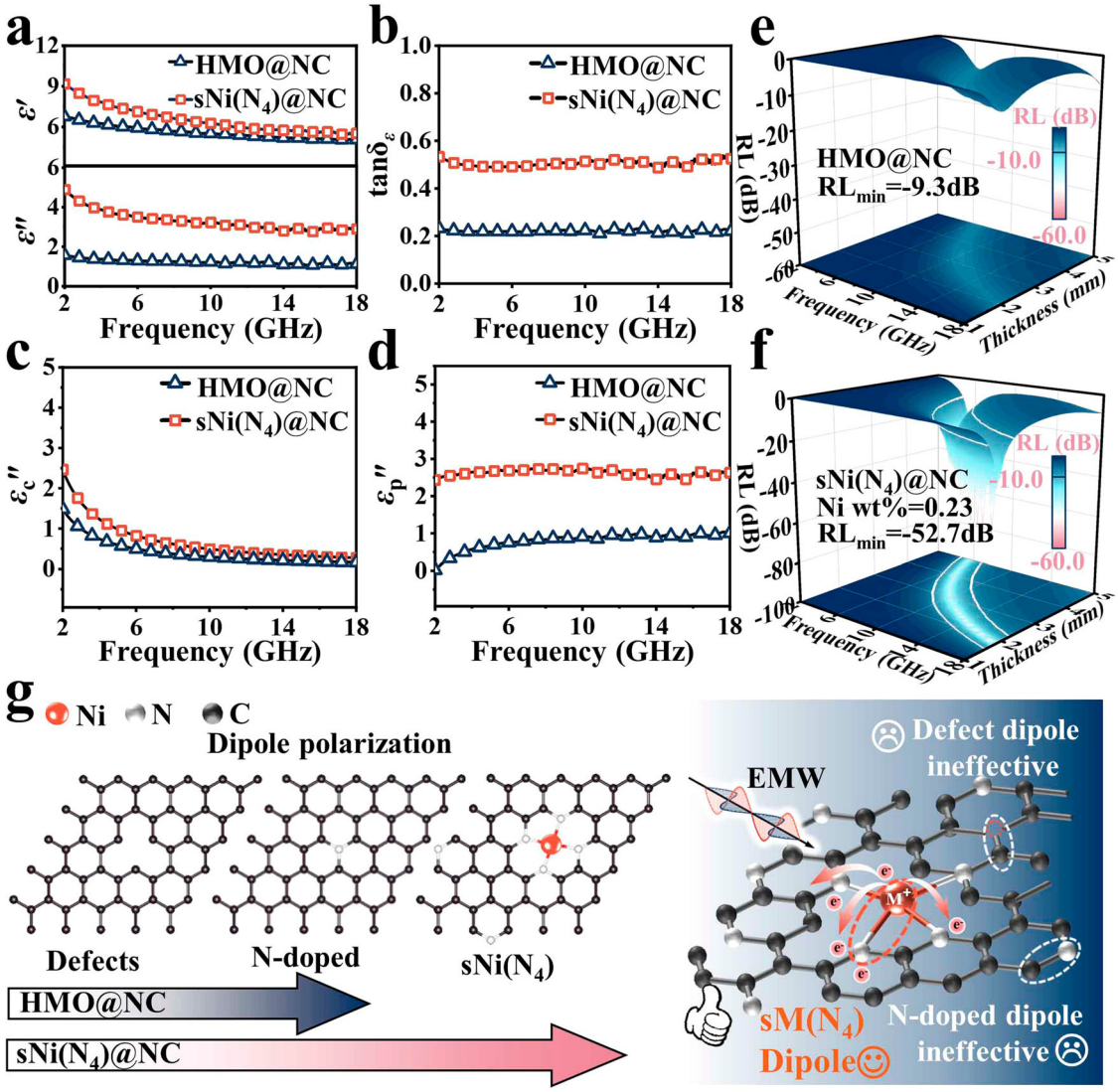

Fig. 3 | EMW absorption measurements. a Real (ε') and imaginary (ε'') parts of permittivity, (**b**) Tan δ_ε, (**c**) Conduction loss (ε_c'') and (**d**) Polarization relaxation loss (ε_p'') of HMO@NC and sNi(N_4)@NC. 3D RL plots of (**e**) HMO@NC and (**f**) sNi(N_4)@NC. **g** Dipole polarization species for HMO@NC and sNi(N_4)@NC (The length of the arrow represents the dipole polarization species contained in the sample).

the HMO@NC materials, transforming them from non-absorbing to highly absorbing.

For studying in-depth EMW dissipation approaches, taking sNi(N_4)@NC (minimum RL and maximum absorption bandwidth of −52.7 dB and 6.08 GHz) into account, the EMW absorption performance of the hollow sNi(N_4)@NC-3 is found to undergo insignificant improvement (minimum RL (RL_{min}) and maximum electromagnetic absorption bandwidth (EAB) of −32.9 dB and 5.68 GHz, respectively). This suggests that HMO plays a role as a support for preparing PPy surface, rather than contributing to the EMW absorption. With regard to HMO@NC, admittedly, it presents no effective absorption bandwidth (Supplementary Fig. 1f–h), which further confirms the above conclusion. To conclude, the EMW absorption of samples with sNi(N_4) is mainly attributed to dipole polarization loss rather than interface polarization. As shown in Fig. 3g, both defective dipoles and N-doped dipoles exist in HMO@NC. However, when sNi(N_4) dipoles are modulated on the surface, the EMW absorption performance of sNi(N_4)@NC is remarkably enhanced. This observation suggests that the sNi(N_4)@NC model elicits a sNi(N_4) dipole polarization loss mechanism and verified that EMW attenuation largely occurs on the EMW absorbers' surfaces.

To examine the universality of (A) the developed sNi(N_4)@NC model; (B) the hypothesis underpinning the sNi(N_4) dipole loss mechanism, we speculated that the EMW absorption performance of sM(N_4)@NC is anticipated to change regularly, an outcome relying upon the metal electronegativities. According to the Allen scale, the electronegativity follows the increasing trend of Co(1.84) <Cu(1.85) <Ni(1.88)[45]; whereas the higher the electronegativity, the stronger the attraction tends to be towards the electrons. Moreover, the conduction loss is only slightly increased with the surface-mounting a small number of single-atoms, which further verified the above conclusion. Therefore, in order to exclude the interference of conduction loss, 30 °C was chosen as the temperature of the click reaction, which is conducive to the accurate study of sNi(N_4) dipole loss mechanism. As one might expect, across the sM(N_4)@NC platform of materials, the minimum RL and maximum bandwidth of −55.9 dB and 4.8 GHz is registered by sCo(N_4)@NC-1, whereas −38.6 dB and 4.6 GHz were recorded for sCu(N_4)@NC-1, higher than those for sNi(N_4)@NC-1 (−17.8 dB and 4.7 GHz). This trend is consitsent with the order of their increasing electronegativity values (Co <Cu <Ni) (Fig. 4a). The difference between the electrogenativity of metal atoms and N shows a good correlation ($R^2 = 0.95$) with

https://doi.org/10.1038/s41467-024-53465-1

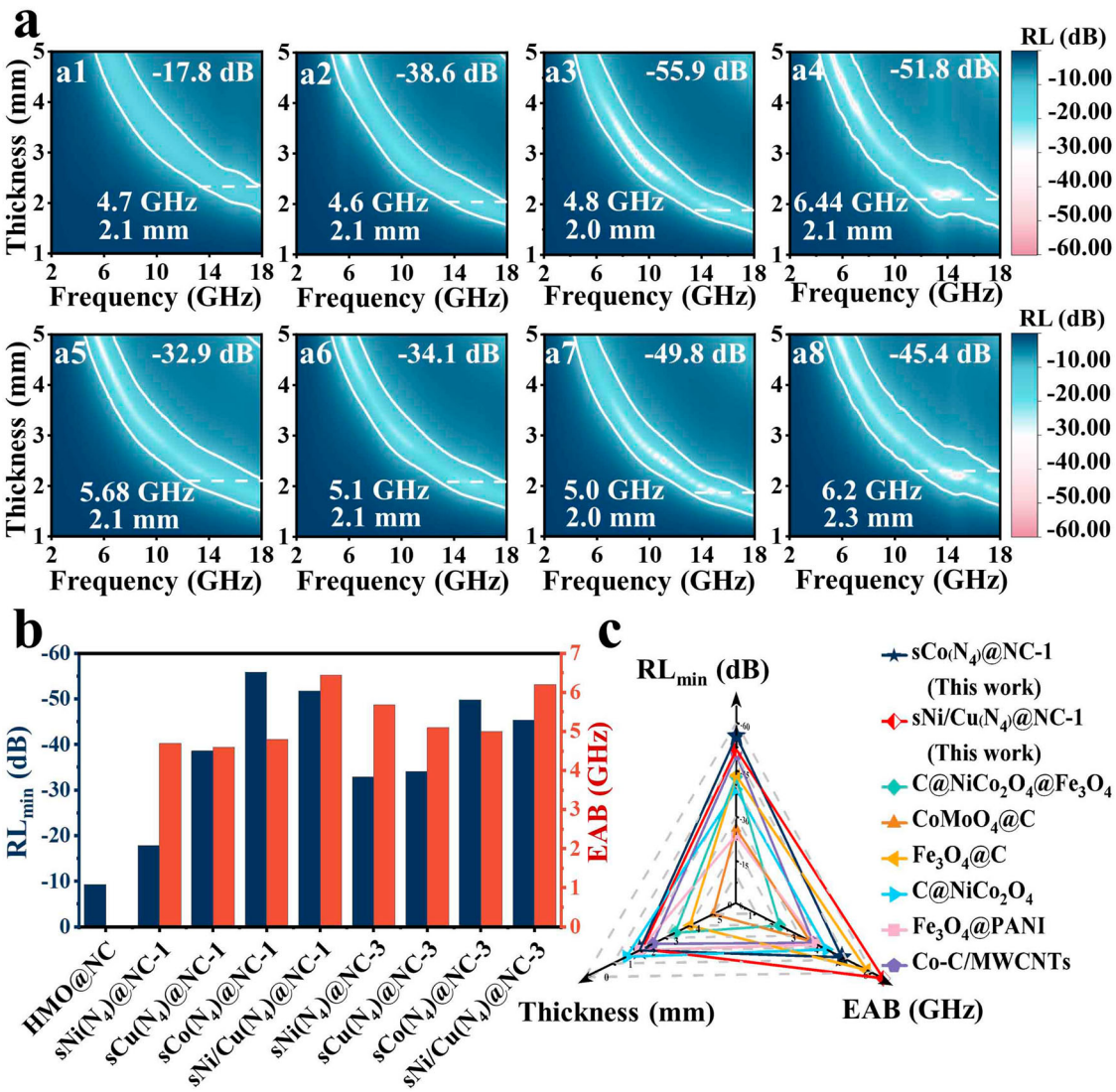

Fig. 4 | EMW absorption properties of sM(N$_4$)@NC with different single metal sites. a 2D reflecting loss (RL) plots of (a1) sNi(N$_4$)@NC-1, (a2) sCu(N$_4$)@NC-1, (a3) sCo(N$_4$)@NC-1, (a4) sNi/Cu(N$_4$)@NC-1, (a5) sNi(N$_4$)@NC-3, (a6) sCu(N$_4$)@NC-3, (a7) sCo(N$_4$)@NC-3 and (a8) sNi/Cu(N$_4$)@NC-3. **b** Summary of RL$_{min}$ and EAB of the samples with different metal single atoms. **c** Comparison of EAB, thickness, and RL$_{min}$ for the EMW absorption performances of some representative carbon-based absorbers.

the corresponding RL$_{min}$, suggesting a unique sM(N$_4$) dipole loss dominated mechanism (Supplementary Fig. 23). These results further indicate that the interfacial polarization between HMO and the carbon layer has little effect on the EMW absorption properties of sM(N$_4$)@NC (M=Ni, Co, Cu, Ni/Cu), and the hollow structure renders a negligible impact on its absorption performance (Fig. 4a, b and Supplementary Table 5). Meanwhile, the contribution of magnetic loss to sM(N$_4$)@NC is also negligible according to the experimental data (Supplementary Fig. 24). Excluding the conductive losses, it was found that sCo(N$_4$)@NC-1 exhibits superior polarization loss capability, consistent with its minimal reflection loss (Supplementary Figs. 25–28). More interestingly, the sM(N$_4$)@NC model can be applied to achieve higher effective EMW absorbers based on the surface modulation of single bimetalic sites. For instance, surface-mouduated single Ni/Cu bimetallic sites on nitrogen-doped carbon surface exhibits the minimum RL and maximum bandwidth of –51.7 and 6.44 (sNi/Cu(N$_4$)@NC-1; thickness = 2.1 mm) (Fig. 4a), which are competitive to the state-of-the-art in EMW absorption application, that is, physically mixed single sites. Additionally, a systematic comparison was conducted *vs*. the previously reported carbon-based EMW absorption benchmarks (Fig. 4c, Supplementary Table 6).

After the complete evaluation of the dissipation approaches and performance of the developed sM(N$_4$)@NC-1 (M = Ni, Co, Cu, Ni/Cu) model, detailed computations were further conducted to explain the dipole polorization loss mechanism. Differential charge densities reinforce the modification of sM(N$_4$) (M = Ni, Co, Cu), causing a redistribution of charges, which in turn disrupts the local microstructure's symmetry[46]. Compared to sNi(N$_4$) and sCu(N$_4$), the modifications in sCo(N$_4$) induce a more significant electronic cloud distortion on the carbon network structure (Fig. 5a and Supplementary Fig. 29). The work function of the energy required to add or remove an electron was calculated to further explain the charge movement in sM(N$_4$)@NC-1[47]. As shown in Fig. 5b, the introduction of sM(N$_4$) leads to a decrease in the overall work function (Φ: NC, 4.387 eV → sNi(N$_4$)@NC-1, 4.371 eV → sCu(N$_4$)@NC-1, 4.335 eV → sCo(N$_4$)@NC-1, 4.285 eV). The decrease in work function weakens the electron binding constraints, enhances the surface band bending, and facilitates carrier migration[48,49]. Theoretically, the charges are more easily attracted to C and N atoms. The carrier behaviors were further analyzed by

https://doi.org/10.1038/s41467-024-53465-1

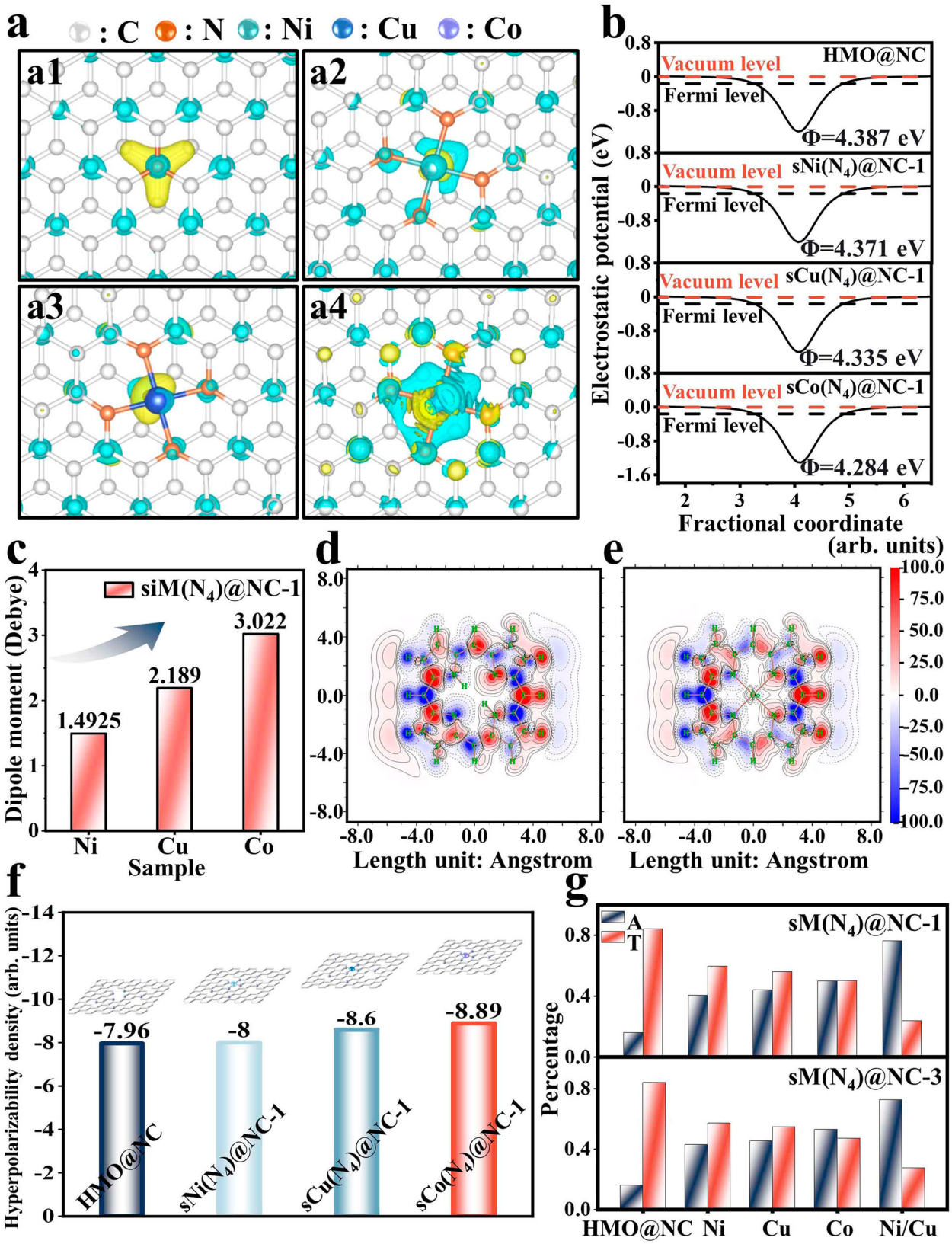

Fig. 5 | DFT calculations and electrochemical detection. a Differential charge densities of (a1) HMO@NC, (a2) sNi(N_4)@NC, (a3) sCu(N_4)@NC, (a4) sCo(N_4)@NC. **b** The work functions of HMO@NC and sM(N_4)@NC (M = Ni, Cu, Co). **c** Dipole moments of sM(N_4)@NC (M = Ni, Cu, Co). Hyperpolarizability densities of (**d**) HMO@NC and (**e**) sCo(N_4)@NC (the red and solid line fragments represent areas where the electric field leads to an increase in density; the blue and dashed line fragments correspond to areas where the electric field leads to a decrease in density). **f** First hyperpolarizability density histograms of HMO@NC and sM(N_4)@NC (M = Ni, Cu, Co) in the x-direction, and (**g**) average values for T and A of all the studied samples (T represents the transmittance of EMW and A represents the absorption rate of EMW).

electrochemically derived Tafel curves. The Tafel plots revealed that surface-modification of single metal atoms leads to a decrease in the Tafel slope, which can be attributed to the improvement of charge carrier behavior (Supplementary Fig. 30a–c). As the loading of $sM(N_4)$ increases and the electronegativity decreases, the overpotential gradually increases, indicating that electrode polarization is primarily caused by dipole polarization induced by $sM(N_4)$ (Supplementary Fig. 30a–c)[50,51]. The electrochemical impedance spectra (EIS) further confirm that the modification of $sM(N_4)$ reduces charge transfer resistance (R_{ct}) (Supplementary Fig. 30d, e). This suggests an order of increasing carrier mobility from $sNi(N_4)$@NC-1 to $sCu(N_4)$@NC-1 to $sCo(N_4)$@NC-1, demonstrating how this trend facilitates interfacial charge transfer[52,53],

Besides, Mulliken charges draw out the charges of N and C atoms in the HMO@NC to be −0.37 and 0.37, respectively. Upon modifying $sM(N_4)$, electrons in the system tend to shift more towards the N and C atoms, resulting in a significant reduction in the charges on N and C atoms in $sM(N_4)$@NC-1 (Supplementary Table 7). In $sCo(N_4)$@NC-1, the charge reduction is the most significant (N: −0.551, C: 0.243), which aligns with the electron cloud distortion caused by Co. In this case, each single-atom site can be regarded as a center of polarization. These polarization centers can prompt polarization losses under alternating electromagnetic fields, thereby enhancing the absorption of electromagnetic waves. As the electronegativity of Co is the lowest, $sCo(N_4)$@NC-1 exhibits the strongest polarization effect, corresponding to the strongest polarization losses and optimal electromagnetic parameters.

The redistribution of charge leads to the formation of dipoles, which incites dipole polarization loss under EMW, and is the primary reason behind the enhanced EMW absorption performance of $sM(N_4)$@NC-1. To investigate the polarization loss performances caused by different metals, we determined the dipole moments for all the samples. As shown in Fig. 5c and Supplementary Table 8, the dipole moments were found to change substantially, and this is likely caused by the redistribution of charges upon introducing $sM(N_4)$. The latter led to an increase in dipole moment along $sNi(N_4)$@NC-1 (1.493 Debye), $sCu(N_4)$@NC-1 (2.189 Debye) and $sCo(N_4)$@NC-1 (3.022 Debye). The increasing dipole moments indicate that the surface modification of $sM(N_4)$ causes distortion of the intrinsic charge density and internal electric field in the space charge region, which facilitates the separation of charge carriers and accelerates charge transfer[54,55]. Besides, enhanced dipole moments promote the formation of a polarizing electric field, resulting in strong macroscopic polarization[56–58].

Polarizability density proportionately quantifies the contribution of each position in 3D space to the polarization rate and the response of different regions in the system under the influence of an external electric field. As shown in Fig. 5d, e and Supplementary Fig. 31, HMO@NC is much less polarized along the direction perpendicular to the electric field compared to $sM(N_4)$@NC-1. This is further corroborated by the increase in polarizability density along HMO@NC (7.96) <$sNi(N_4)$@NC-1 (8.00) <$sCu(N_4)$@NC-1 (8.60) <$sCo(N_4)$@NC-1 (8.89) (Fig. 5f). In this case, $sCo(N_4)$@NC-1 possesses larger dipole moment and polarizability, exhibits better polarization loss *vs.* the losses observed in $sNi(N_4)$@NC-1 and $sCu(N_4)$@NC-1. Combining the experimental and theoretical results, it is reasonable to conclude that the $sM(N_4)$@NC model has generated a unique $sNi(N_4)$ dipole polarization loss mechanism. This approach further strengthened our hypothesis that EMW attenuation mainly occurs on the EMW absorber surface. The radar cross section (RCS) simulation results obtained by FEKO software further verify the effective enhancement of EMW absorption performance of $sM(N_4)$@NC-1 by surface modification of $sM(N_4)$ (Supplementary Figs. 32–35 and Supplementary Tables 9, 10).

Discussion

In summary, we present a previously unreported surface modulation strategy that anchors metal atoms, surrounded by 4 nitrogen atoms, onto a nitrogen-doped carbon layer. Our results demonstrate that this surface modulation can trigger a unique dipole polarization loss mechanism with record-high EMW absorption performance. $sNi(N_4)$@NC exhibits highly promising EMW absorption properties, with its minimum reflection loss and maximum absorption bandwidth surpassing the performances of the state-of-the-art materials, which are often based on single atoms and/or carbonaceous compositions. A series of experimental and theoretical characterizations confirmed the EMW absorption mechanism, focusing on the interfacial polarization of HMO and NC, while ruling out the influence of N-doped and defective dipoles on the NC surface. The high EMW absorption performance of $sM(N_4)$@NC (M = Ni, Cu, Co, Ni/Cu) is ascribed to the polarization loss mechanism of the MN_4 diploes. Moreover, the EMW absorption ability can be optimized by fine-tuning the monometallic (substituting Ni with Cu or Co) and bimetallic compositions (Ni/Cu clusters), exemplifying bottom-up control.

Overall, this dipole polarization loss mechanism, which enables unprecedented EMW absorption, and the structure-property relationships arising from the electronegativities of the metal atoms, offer new routes for designing the next-generation EMW absorbers with atomistic precision.

Methods

Chemicals

Pyrrole, potassium peroxodisulfate ($K_2S_2O_8$), nickel chloride hexahydrate ($NiCl_2{\cdot}6H_2O$), cobalt chloride hexahydrate ($CoCl_2{\cdot}6H_2O$), copper chloride dehydrate ($CuCl_2{\cdot}2H_2O$) and *N*,*N*-dimethylformamide (DMF) were purchased from Macklin (Shanghai, China). *Meso*-tetra(4-phenyl) porphine(Por), potassium hydroxide (KOH), triethylamine, thionyl chloride ($SOCl_2$), tetrahydrofuran (THF) and 4-dimethylaminopyridine (DMAP) were acquired from Aladdin (Shanghai, China). All chemicals were of analytical grade, and used as received.

Characterization

High-resolution transmission electron microscope (TEM, JEM-2100, JEOL) equipped with an energy dispersive spectrometer (EDS) was utilized to investigate the morphology and structure of the samples and perform elemental mapping analysis. PXRD patterns were recorded on a Bruker D8 diffractometer using Cu Kα radiation (λ = 1.5406 Å) with a scanning range of $5° < 2\theta < 80°$. FTIR was performed on NICOLET IS 20 spectrograph. X-ray photoelectron spectroscopy (XPS) information were recorded by a PHI 5000 VersaProbe system with an Al Kα X-ray source at 150 W. Raman spectra were recorded on a Raman spectrophotometer (Aramis) with a 532 nm solid laser as an excitation source (200 ~ 4000 cm^{-1}). Inductively coupled plasma optical emission spectroscopic data (ICP-OES, NEXSA, iCAPRQ) was recorded to detect the Ni content in the samples. Conductivity of the prepared samples was detected by four-point probe (RTS-8). The electrochemical performance was detected by a CHI 660E electrochemical workstation. A three-electrode cell conFigureuration was employed and all samples should be coated on a glassy carbon electrode as working electrodes in the additive of carbon black and polyvinylidene fluoride in a mass ratio of 24:4:3. Additionally, a saturated silver chloride electrode, a Pt wire, and 1 M Na_2SO_4 aqueous solution was employed as reference electrode, counter electrode, and electrolyte, respectively.

X-ray Absorption Fine Structure measurement

Ni K-edge XAFS measurements were conducted at the BL14W beamline of the Shanghai Synchrotron Radiation Facility (SSRF), P. R. China. Prior to the beamline measurement, samples were secured in aluminum holders and sealed with Kapton tape. A Bruker 5040 4-channel

Silicon Drift Detector (SDD) was used to monitor the XAFS spectra at room temperature. Transmission/fluorescence mode was employed to record Ni K-edge EXAFS spectra. The line-shape and peak position of Ni K-edge XANES spectra exhibited negligible variations between two scans for a particular sample. The standard samples' XAFS spectra of such as NiPc, Ni-foil, and NiO were obtained in transmission mode. The spectra were processed and analyzed by the software codes Athena.

Electromagnetic measurements

Utilizing a vector network (N5222B) analyzer to record the electromagnetic parameters containing complex permittivity ($\varepsilon_r = \varepsilon' - j\varepsilon''$) and permeability ($\mu_r = \mu' - j\mu''$) by a typical coaxial-line method. Beforehand, all samples (40 wt%) were pressed into rings-like (Φ_{in} = 3.04 mm, Φ_{out} = 7.00 mm) in paraffin. The EMA performance can be calculated according to following equations[59].

$$RL(dB) = 20\log_{10}\frac{|z_{in} - z_0|}{|z_{in} + z_0|} \quad (1)$$

$$z_{in} = z_0\sqrt{\frac{\mu_r}{\varepsilon_r}}\tanh\left(\frac{2\pi jfd}{c}\sqrt{\mu_r\varepsilon_r}\right) \quad (2)$$

Where Z_{in}, Z_0, f, d and c represent impedance of absorbers, impedance of free-space, incident EMW frequency, thickness of absorbers and velocity of light.

Frequency domain simulation of the radar cross-section (RCS)

The RCS simulation were performed by FEKO 2020 software, using a metal back and a Predator 2 as models. For the metal back, simulation I) simulation model was composed of a bottom PEC plate (200 mm * 200 mm * 1 mm) and an upper coating (sM(N_4)@NC, 3.00 mm). The model was in the XOY plane, and the open (add space) boundary conditions were used in all directions. The scattering directions were set as ≈ −90–90° for theta (θ), and 0–360° for phi (φ), and the monitor frequency was set as 9.04 GHz. Simulation II) simulation model was composed of a bottom PEC plate (200 mm * 200 mm * 1 mm) and an upper coating (sM(N_4)@NC, 4.40 mm). The model was in the XOY plane, and the open (add space) boundary conditions were used in all directions. The scattering directions were set as ≈ −90–90° for theta (θ), and 0–360° for phi (φ), and the monitor frequency was set as 6.08 GHz.

For the Predator 2, simulation model was made up of and a bottom PEC layer and an upper absorbing layer (sCo(N_4)@NC, 3.00 mm). The model was in the XOY plane, and the open (add space) boundary conditions were used in all directions. 0°, 45°, and 90° were selected as the detection angle (θ) for simulation, and the scattering directions were set as ≈0–360° for phi (φ). The monitor frequency was set as 9.04 GHz.

Density functional theory (DFT) calculation

In this study, Density Functional Theory (DFT) calculations were conducted using the CP2K software[60]. A two-dimensional NC-M (M: Ni, Cu and Co) model was constructed, and an 8 Å vacuum layer was included in the model. To replicate real-world scenarios, vacancies were introduced by removing specific carbon atoms within the model. Furthermore, the model incorporated nitrogen substitutions at specific carbon sites.

These computations were conducted utilizing the PBE density functional[61] and the DZVP-MOLOPT-SR-GTH[62] basis set. The kinetic energy cutoff was set to be 600 eV, and the total energy convergence was set as 10^{-6} eV for self-consistent iterations. A judiciously implemented smearing technique permeated the entirety of the calculations, maintaining an electronic temperature of 300 Kelvin (K).

Synthesis of HMO@NC-0.5, HMO@NC and HMO@NC-2

H-MoO_3 (HMO) was prepared following the methodology established in previous research[63]. Then, 2 g HMO was dissolved in a mixture of 100 ml deionized water and 100 ml ethanol, and sonicated for 20 min. The solution was placed in the refrigerator at −80 °C for 10 minutes. Afterwards, x (x = 1, 2 and 4) g pyrrole and x (x = 4, 8 and 12) g $K_2S_2O_8$ were added to the above solution, respectively. The mixture was stirred for 6 h at room temperature. The precipitate was filtered and washed six times with deionized water and ethanol. The samples obtained were dried overnight in vacuum, and labeled as HMO@PPy-0.5, HMO@PPy and HMO@PPy-2, respectively. After that, the samples were pyrolyzed at 700 °C for 3 h under Ar atmosphere with a heating rate of 5 °C/min and the samples obtained was labeled as HMO@NC-0.5, HMO@NC and HMO@NC-2, respectively.

Synthesis of NiPor, CuPor and CoPor

0.854 g Meso-tetra(4phenyl)porphine (Por) and 3.1 g $NiCl_2{\cdot}6H_2O$ were dissolved in 100 ml of DMF and the solution was heated to reflux at 140 °C for 6 h. Then, add 150 ml of deionized water to above solution and the solid was obtained by filtration. Firstly, wash the obtained solid three times with 1 M HCl, and then wash it three times with deionized water. The purple solid was collected by filtration, and dried overnight in vacuum.

0.75 g purple solid was dissolved in a mixture of 25 ml THF and 25 ml methanol and 25 ml of KOH solution (2.63 g) was slowly added. The mixture was heated to reflux at 85 °C for 24 h. After the reaction is finished and cooled to room temperature, enough deionized water was added to dissolve the solid completely. The reaction solution was then acidified by slow dropwise addition of 1 M HCl until no excess precipitate was generated in the system. The rufous solid was obtained by filtration and washing with plenty of water. The product was labeled as NiPor, CuPor and CoPor were prepared by similar methods.

Synthesis of sNi(N_4)@NC and sNi(N_4)@NC-X (X: 1, 2 and 3)

In general, NiPor was covalently grafted onto HMO@PPy via an amidation reaction at 30 °C, 60 °C, 80 °C and 100 °C, respectively. Specifically, by dissolving NiPor (200 mg) and $SOCl_2$ (68 μl) in 15 mL of DMF for 10 min with sonication. The carboxyl groups were then converted to acyl chloride. The catalyst DMAP (115 mg) for further amidation was then added to the above solution to form the feedstock solution. In addition, HMO@PPy (200 mg) was dispersed in a solution of DMF (30 mL) containing 346 μL of triethylamine and sonicated for 45 min to form a homogeneous suspension. Finally, the feedstock solution was added dropwise to the homogeneously dispersed HMO@PPy suspension. The mixture was stirred separately for 24 h under 30 °C, 60 °C, 80 °C and 100 °C, respectively. After cooling to room temperature, the black particles were filtered and washed six times alternately with DMF and ethanol. The obtained samples were dried in vacuum at 60 °C for 12 h to afford sNi(N_4)@PPy, sNi(N_4)@PPy-60, sNi(N_4)@PPy-80 and sNi(N_4)@PPy-100. Then, the samples were pyrolyzed at 700 °C for 3 h under Ar atmosphere with a heating rate of 5 °C/min and the samples obtained was labeled as sNi(N_4)@NC-1, sNi(N_4)@NC-2, sNi(N_4)@NC and sNi(N_4)@NC-3, respectively.

Synthesis of sCu(N_4)@NC-1 and sCu(N_4)@NC-3

In general, by dissolving CuPor (200 mg) and $SOCl_2$ (68 μl) in 15 mL of DMF for 10 min with sonication. The carboxyl groups were then converted to acyl chloride. The catalyst DMAP (115 mg) for further amidation was then added to the above solution to form the feedstock solution. In addition, HMO@PPy (200 mg) was dispersed in a solution of DMF (30 mL) containing 346 μL of triethylamine and sonicated for 45 min to form a homogeneous suspension. Finally, the feedstock solution was added dropwise to the homogeneously dispersed HMO@PPy suspension. The mixture was stirred separately for 24 hours under 30 °C and 100 °C, respectively. After cooling to room

temperature, the black particles were filtered and washed six times alternately with DMF and ethanol. The obtained samples were dried in vacuum at 60 °C for 12 h to afford sCu(N_4)@PPy and sCu(N_4)@PPy-100. Then, the samples were pyrolyzed at 700 °C for 3 h under Ar atmosphere with a heating rate of 5 °C/min and the samples obtained was labeled as sCu(N_4)@NC-1 and sCu(N_4)@NC-3, respectively.

Synthesis of sCo(N_4)@NC-1 and sCo(N_4)@NC-3

In general, by dissolving CoPor (200 mg) and $SOCl_2$ (68 μl) in 15 mL of DMF for 10 min with sonication. The carboxyl groups were then converted to acyl chloride. The catalyst DMAP (115 mg) for further amidation was then added to the above solution to form the feedstock solution. In addition, HMO@PPy (200 mg) was dispersed in a solution of DMF (30 mL) containing 346 μL of triethylamine and sonicated for 45 min to form a homogeneous suspension. Finally, the feedstock solution was added dropwise to the homogeneously dispersed HMO@PPy suspension. The mixture was stirred separately for 24 h under 30 °C and 100 °C, respectively. After cooling to room temperature, the black particles were filtered and washed six times alternately with DMF and ethanol. The obtained samples were dried in vacuum at 60 °C for 12 h to afford sCo(N_4)@PPy and sCo(N_4)@PPy-100. Then, the samples were pyrolyzed at 700 °C for 3 h under Ar atmosphere with a heating rate of 5 °C/min and the samples obtained was labeled as sCo(N_4)@NC-1 and sCo(N_4)@NC-3, respectively.

Synthesis of sNi/Cu(N_4)@NC-1 and sNi/Cu(N_4)@NC-3

In general, by dissolving NiPor (100 mg), CuPor (100 mg) and $SOCl_2$ (68 μl) in 15 mL of DMF for 10 min with sonication. The carboxyl groups were then converted to acyl chloride. The catalyst DMAP (115 mg) for further amidation was then added to the above solution to form the feedstock solution. In addition, HMO@PPy (200 mg) was dispersed in a solution of DMF (30 mL) containing 346 μL of triethylamine and sonicated for 45 min to form a homogeneous suspension. Finally, the feedstock solution was added dropwise to the homogeneously dispersed HMO@PPy suspension. The mixture was stirred separately for 24 h under 30 °C and 100 °C, respectively. After cooling to room temperature, the black particles were filtered and washed six times alternately with DMF and ethanol. The obtained samples were dried in vacuum at 60 °C for 12 h to afford sNi/Cu(N_4)@PPy and sNi/Cu(N_4)@PPy-100. Then, the samples were pyrolyzed at 700 °C for 3 h under Ar atmosphere with a heating rate of 5 °C/min and the samples obtained was labeled as sNi/Cu(N_4)@NC-1 and sNi/Cu(N_4)@NC-3, respectively.

Data availability

All relevant data are available within the article and Supplementary information. Any additional requests for information can be directed to and will be fulfilled by the corresponding authors. Source data are provided with this paper.

References

1. Liu, L. et al. Interactions between electromagnetic radiation and biological systems. *iScience* **27**, 109201 (2024).
2. Liu, L. et al. Specific electromagnetic radiation in the wireless signal range increases wakefulness in mice [Neuroscience]. *Proc. Natl. Acad. Sci. USA* **118**, e2105838118 (2021).
3. Gulati, S. et al. Phenotypic and genotypic characterization of antioxidant enzyme system in human population exposed to radiation from mobile towers. *Mol. Cell. Biochem.* **440**, 1–9 (2018).
4. Shu, R. et al. Nitrogen-doped Co-C/MWCNTs nanocomposites derived from bimetallic metal–organic frameworks for electromagnetic wave absorption in the X-band. *Chem. Eng. J.* **362**, 513 (2019).
5. Wu, C. et al. Hollow gradient-structured iron-anchored carbon nanospheres for enhanced electromagnetic wave absorption. *Nano-Micro Lett.* **15**, 7 (2023).
6. Rehman, H. et al. Fragmented graphene synthesized on a dielectric substrate for THz applications. *NanoTechnology* **33**, 395703 (2022).
7. Cao, M. et al. Thermally driven transport and relaxation switching self-powered electromagnetic energy conversion. *Small* **14**, 1800987 (2018).
8. Li, B. et al. Graphene-assisted assembly of electrically and magnetically conductive ceramic nanofibrous aerogels enable multifunctionality. *Adv. Funct. Mater.* **34**, 2314653 (2024).
9. Li, C. et al. The rambutan-like C@$NiCo_2O_4$ composites for enhanced microwave absorption performance. *J. Mater. Sci. Mater. Electron.* **30**, 3124 (2019).
10. Zhai, N. et al. Interface engineering of heterogeneous $NiSe_2$-$CoSe_2$@C@$MoSe_2$ for high-efficient electromagnetic wave absorption. *Adv. Funct. Mater.* **34**, 2312237 (2024).
11. Zhao, B. et al. A liquid-metal-assisted competitive galvanic reaction strategy toward Indium/Oxide core–shell nanoparticles with enhanced microwave absorption. *Adv. Funct. Mater.* **34**, 2314008 (2024).
12. Yang, W. et al. Construction and microwave absorption properties of core@double-shell structured Fe_3O_4@polyaniline@MnO_2. *Nanospheres. Nano* **15**, 2050032 (2020).
13. Fu, C. et al. Enhanced microwave absorption properties of polyaniline-modified porous Fe_3O_4@C nanosheets. *J. Mater. Sci. Mater. Electron.* **30**, 11907 (2019).
14. Wei, S. et al. Preparation of hierarchical core-shell C@$NiCo_2O_4$@Fe_3O_4 composites for enhanced microwave absorption performance. *Chem. Eng. J.* **314**, 477 (2017).
15. Zhao, B. et al. A Liquid-metal-assisted competitive galvanic reaction strategy toward Indium/Oxide core–shell nanoparticles with enhanced microwave Absorption. *Adv. Funct. Mater.* **34**, 2314008 (2024).
16. Wu, Z. et al. Dimensional design and core–shell engineering of nanomaterials for electromagnetic wave absorption. *Adv. Mater.* **34**, 2107538 (2022).
17. Liang, H. Exploring the Ni 3d orbital unpaired electrons induced polarization loss based on Ni single-atoms model absorber. *Adv. Funct. Mater.* **33**, 2212604 (2023).
18. Xu, J. et al. Atomically dispersed cobalt anchored on N-doped graphene aerogels for efficient electromagnetic wave absorption with an ultralow filler ratio. *Appl. Phys. Rev.* **9**, 011402 (2022).
19. Lv, X. et al. Tunable surface chemistry in heterogeneous bilayer single-atom catalysts for electrocatalytic NO_x reduction to ammonia. *Adv. Funct. Mater.* **32**, 2201262 (2022).
20. Liu, H. et al. Large annular dipoles bounded between single-atom Co and Co cluster for clarifying electromagnetic wave absorbing mechanism. *Adv. Funct. Mater.* **33**, 2304442 (2023).
21. Liang, L. et al. Heterointerface engineering in electromagnetic absorbers: new insights and opportunities. *Adv. Mater.* **34**, 2106195 (2022).
22. Huang, M. et al. Heterogeneous interface engineering of Bi-Metal MOFs-derived $ZnFe_2O_4$–ZnO-Fe@C microspheres via confined growth strategy toward superior electromagnetic wave absorption. *Adv. Funct. Mater.* **34**, 2308898 (2023).
23. Li, W. et al. Unprecedented high oxygen evolution activity of electrocatalysts derived from surface-mounted metal–organic frameworks. *J. Am. Chem. Soc.* **141**, 5926 (2019).
24. Hou, S. et al. Metamorphosis of heterostructured surface-mounted metal–organic frameworks yielding record oxygen evolution mass activities. *Adv. Mater.* **33**, 2103218 (2021).
25. Li, W. et al. In situ tracking of wetting-front transient heat release on a surface-mounted metal–organic framework. *Adv. Mater.* **33**, 2006980 (2021).
26. Hou, M. et al. Microenvironment reconstitution of highly active Ni single atoms on oxygen-incorporated Mo_2C for water splitting. *Nat. Commun.* **15**, 1342 (2024).

27. Gong, Y. et al. Regulating the coordination environment of MOF-templated single-atom nickel electrocatalysts for boosting CO_2 reduction. *Angew. Chem. Int. Ed.* **59**, 2705 (2020).
28. Yang, X. F. et al. Single-atom catalysts: a new frontier in heterogeneous catalysis. *Acc. Chem. Res.* **46**, 1740–1748 (2013).
29. Ding, J. et al. Atomic high-spin cobalt(II) center for highly selective electrochemical CO reduction to CH_3OH. *Nat. Commun.* **14**, 6550 (2023).
30. Zhao, C. et al. A clicking confinement strategy to fabricate transition metal single-atom sites for bifunctional oxygen electrocatalysis. *Sci. Adv.* **8**, eabn5091 (2022).
31. Fan, M. et al. Improving the catalytic activity of carbon-supported single atom catalysts by polynary metal or heteroatom doping. *Small* **16**, 1906782 (2020).
32. Zhao, B. et al. Transformation of 2D flakes to 3D hollow bowls: Matthew effect enables defects to prevail in electromagnetic wave absorption of hollow rGO bowls. *Small* **20**, 2208135 (2023).
33. Zhu, C. et al. CO_2-assisted fabrication of novel heterostructures of h-MoO_3/1T-MoS_2 for enhanced photoelectrocatalytic performance. *Appl. Surf. Sci.* **425**, 56 (2017).
34. Kumar, V. et al. Formation of hexagonal-molybdenum trioxide (h-MoO_3) nanostructures and their pseudocapacitive behavior. *Nanoscale* **7**, 11777 (2015).
35. Choi, Y. et al. Effect of impurities on the corrosion behavior of CO_2 transmission pipeline steel in supercritical CO_2–water environments. *Environ. Sci. Technol.* **44**, 9233–9238 (2010).
36. Fan, W. et al. Rational design of heterogenized molecular phthalocyanine hybrid single-atom electrocatalyst towards two-electron oxygen reduction. *Nat. Commun.* **14**, 1426 (2023).
37. Xie, A. et al. Enhancing electromagnetic absorption performance of Molybdate@Carbon by metal ion substitution. *J. Mater. Sci. Technol.* **163**, 92 (2023).
38. Tian, H. et al. High durability of Fe–N–C single-atom catalysts with carbon vacancies toward the oxygen reduction reaction in alkaline media. *Adv. Mater.* **35**, 2210714 (2023).
39. Zhang, C. et al. A pentagonal defect-rich metal-free carbon electrocatalyst for boosting acidic O_2 reduction to H_2O_2 production. *J. Am. Chem. Soc.* **145**, 11589 (2023).
40. Tu, H. et al. Electronic asymmetry engineering of Fe–N–C electrocatalyst via adjacent carbon vacancy for boosting oxygen reduction reaction. *Adv. Sci.* **10**, 2305194 (2023).
41. Liu, J. et al. A competitive reaction strategy toward binary metal sulfides for tailoring electromagnetic wave absorption. *Adv. Funct. Mater.* **31**, 2105018 (2021).
42. Gao, T. et al. Sub-nanometer Fe clusters confined in carbon nanocages for boosting dielectric polarization and broadband electromagnetic wave absorption. *Adv. Funct. Mater.* **32**, 2204370 (2022).
43. Gao, Z. et al. Cationic etching of ZIF-67 derived $LaCoO_3$/Co_3O_4 as high-efficiency electromagnetic absorbents. *Chem. Eng. J.* **421**, 127829 (2021).
44. Zhang, X. et al. Identification of the intrinsic dielectric properties of metal single atoms for electromagnetic wave absorption. *Nano-Micro Lett.* **14**, 27 (2021).
45. Mann, J. et al. Configuration energies of the d-block elements. *J. Am. Chem. Soc.* **122**, 5132 (2000).
46. Yin, Q. et al. Metallization-prompted robust rorphyrin-based hydrogen-bonded organic frameworks for photocatalytic CO_2 reduction. *Angew. Chem.* **61**, e202115854 (2021).
47. Jin, X. et al. Electron configuration modulation of nickel single atoms for elevated photocatalytic hydrogen evolution. *Angew. Chem.* **132**, 6894 (2020).
48. Dai, Z. et al. Crystal defect engineering of aurivillius Bi_2MoO_6 by Ce doping for increased reactive species production in photocatalysis. *ACS Catal.* **6**, 3180 (2016).
49. Meng, Q. et al. High-efficiency Fe-mediated Bi_2MoO_6 nitrogen-fixing photocatalyst: reduced surface work function and ameliorated surface reaction. *Appl. Catal. B* **256**, 117781 (2019).
50. Gao, Z. et al. Simultaneous manipulation of interfacial and defects polarization toward Zn/Co phase and ion hybrids for electromagnetic wave absorption. *Adv. Funct. Mater.* **31**, 2106677 (2021).
51. Zhang, R. et al. Engineering Cobalt defects in cobalt oxide for highly efficient electrocatalytic oxygen evolution. *ACS Catal.* **8**, 3803 (2018).
52. Zhu, Y. et al. Improving the activity for oxygen evolution reaction by tailoring oxygen defects in double perovskite oxides. *Adv. Funct. Mater.* **29**, 1901783 (2019).
53. Zhang, J. et al. Electro-reconstruction-induced strain regulation and synergism of Ag-In-S toward highly efficient CO_2 electrolysis to formate. *Adv. Funct. Mater.* **32**, 2113075 (2022).
54. Wang, Y. et al. Ni doping in unit cell of BiOBr to increase dipole moment and induce spin polarization for promoting CO_2 photoreduction via enhanced build-in electric field. *Catal. B* **327**, 122420 (2023).
55. Yang, Z. et al. Facial construction of hydroxyl functional modified ultrafine $BiPO_4$ with variation of dipole moment induced by –OH group. *Small Struct.* **5**, 2300339 (2023).
56. Banerjee, T. et al. Polymer photocatalysts for solar-to-chemical energy conversion. *Nat. Rev. Mater.* **6**, 168 (2021).
57. Wang, H. et al. Excitonic effects in polymeric photocatalysts. *Angew. Chem.* **59**, 22828 (2020).
58. Zhang, W. et al. Polarization engineering of conjugated microporous polymers to boost exciton dissociation by dielectric constant regulation for photocatalytic degradation of antibiotics. *Sep. Purif. Technol.* **332**, 125776 (2024).
59. Liang, L. et al. Multifunctional magnetic $Ti_3C_2T_x$ MXene/graphene aerogel with superior electromagnetic wave absorption performance. *ACS Nano* **15**, 6622 (2021).
60. Kühne, T. D. et al. CP2K: An electronic structure and molecular dynamics software package - Quickstep: Efficient and accurate electronic structure calculations. *J. Chem. Phys.* **152**, 194103 (2020).
61. Perdew, J. P., Burke, K. & Ernzerhof, M. Generalized gradient approximation made simple. *Phys. Rev. Lett.* **77**, 3865 (1996).
62. VandeVondele, J. & Gaussian, J. Hutter basis sets for accurate calculations on molecular systems in gas and condensed phases. *J. Chem. Phys.* **127**, 114105 (2007).
63. Cheng, S. et al. Tuning electromagnetic absorption properties of transition metal oxides by hydrogenation with nascent hydrogen. *Chem. Eng. J.* **417**, 127980 (2021).

Acknowledgements

This work was supported by the National Natural Science Foundation of China (52273267 to A.M.X., 22271155 to W.J.L., 22220102005 to R.C.), and the Fundamental Research Funds for the Central Universities (NO. 30922010203 to W.J.L., NO. 2023203001 to W.J.L.), and SFI-IRC Pathway award (21/PATH-S/9454 to S.M.) from the Science Foundation Ireland (SFI). We thank Prof. Lasheng Long from Xiamen University for the fruitful discussions and suggestions.

Author contributions

W.J.L. and A.M.X. directed and supervised the overall project and co-wrote the manuscript. S.Y.C., A.M.X., and W.J.L. conceived and designed the project. S.Y.C. and D.H.S. carried out most of the experiments, analyzed the data and co-wrote the manuscript. W.D., S.M., Y.B.H., R.C., and R.A.F. conducted data curation and reviewed & edited the manuscript. All the authors contributed to the analysis and interpretation of the data.

Competing interests
The authors declare no competing interests.

Additional information
Supplementary information The online version contains supplementary material available at https://doi.org/10.1038/s41467-024-53465-1.

Correspondence and requests for materials should be addressed to Aming Xie or Weijin Li.

Peer review information *Nature Communications* thanks the anonymous reviewer(s) for their contribution to the peer review of this work. A peer review file is available.